

Nearly Exclusive Growth of Small Diameter Semiconducting Single-Wall Carbon Nanotubes from Organic Chemistry Synthetic End-Cap Molecules

Bilu Liu¹, Jia Liu¹, Hai-Bei Li², Radha Bhola³, Edward A. Jackson³, Lawrence T. Scott³, Alister Page⁴, Stephan Irle⁵, Keiji Morokuma⁶, Chongwu Zhou^{1*}

1. Department of Electrical Engineering and Department of Chemistry, University of Southern California, Los Angeles, California, 90089, United States

2. School of Ocean, Shandong University, Weihai 264209, China

3. Merkert Chemistry Center, Boston College, Chestnut Hill, Massachusetts 02467, United States

4. Newcastle Institute for Energy and Resources, The University of Newcastle, Callaghan 2308, Australia

5. WPI-Institute of Transformative Bio-Molecules (ITbM) & Department of Chemistry, Graduate School of Science, Nagoya University, Nagoya 464-8602, Japan

6. Fukui Institute for Fundamental Chemistry, Kyoto University, Kyoto, 606-8103, Japan

Corresponding author chongwuz@usc.edu (C. Z.)

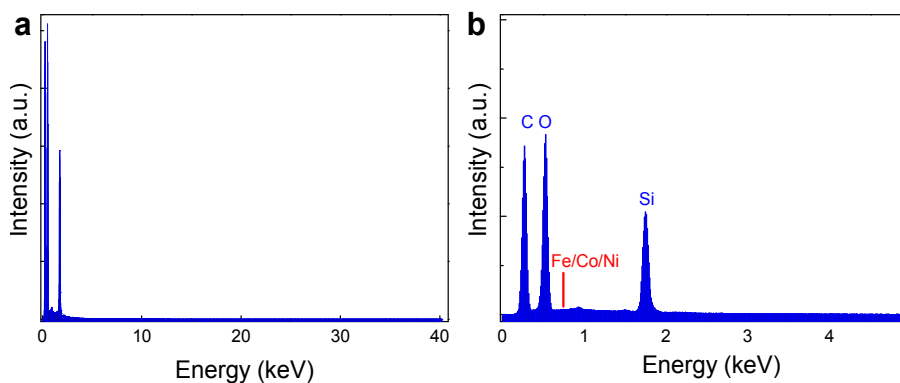


Figure S1 Energy dispersive X-ray (EDX) spectra (Figure S1a) of the $C_{50}H_{10}$ molecules deposited on quartz. For sample preparation, $\sim 10 \mu\text{l}$ of $C_{50}H_{10}$ in toluene was deposited on quartz and kept until dry to obtain thick deposits. The C signal comes from $C_{50}H_{10}$ molecules while the O and Si come from the quartz substrate. Zoom in spectrum in Figure S1b shows that there are no metal elements like Fe, Co, Ni detected.

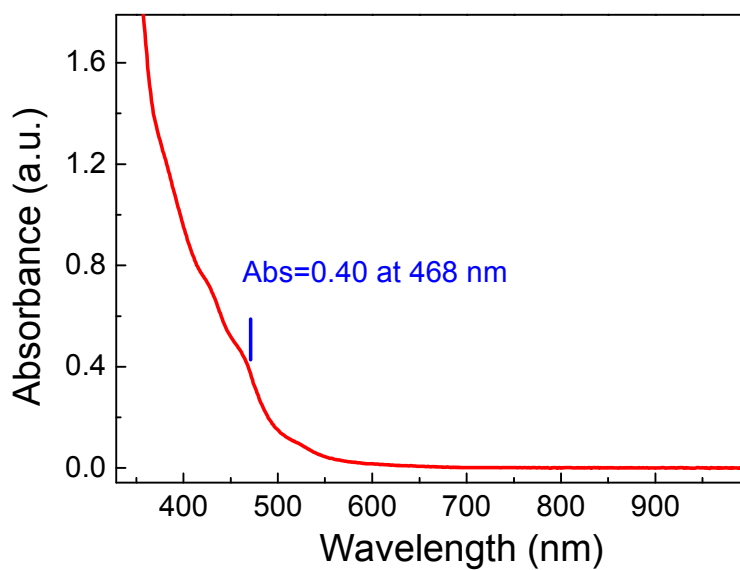


Figure S2 An optical absorption spectrum of the $C_{50}H_{10}$ molecules dissolved in toluene. A solution with absorbance of 0.40 at 468 nm was used in this study.

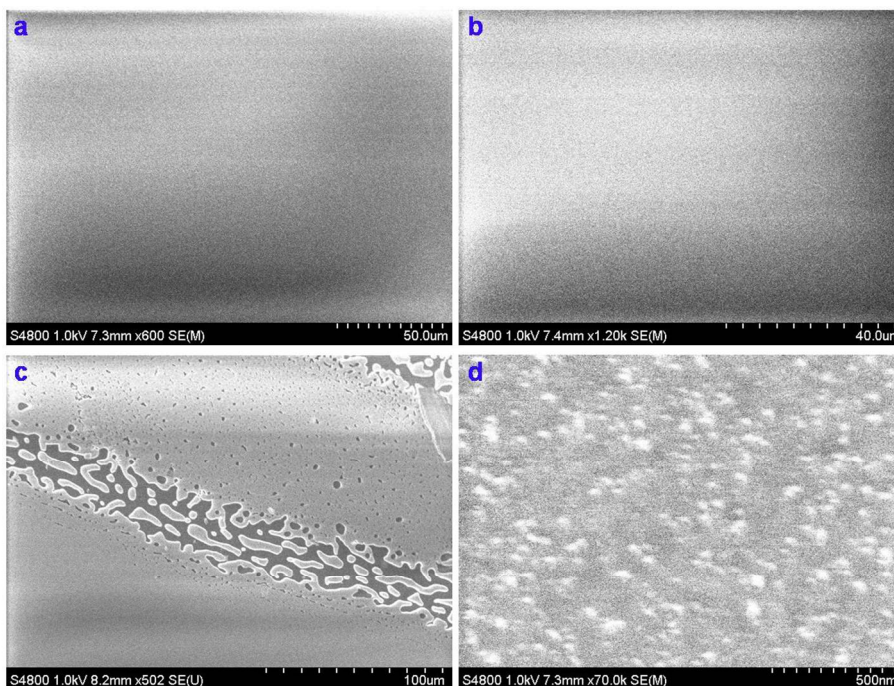


Figure S3 Representative SEM images of the quartz substrate coated with $C_{50}H_{10}$ molecules after the CVD process without seed pretreatment. In these experiments, we systematically studied and varied the growth temperatures (from 700 °C to 975 °C), flow rates of $CH_4/H_2/C_2H_4$ (1300/300/0 sccm, 1300/300/10 sccm, 50/50/10 sccm, 50/100/0 sccm, 50/100/2 sccm, 50/100/5 sccm, 500/100/5 sccm, etc.) and consequently their partial pressures, and growth times (from tens of seconds to 1 hour). The top two images (Figure S3a and S3b) show clean substrates without anything grown on it, whereas the bottom two images (Figure S3c and S3d) show dirty substrates with amorphous carbon deposits.

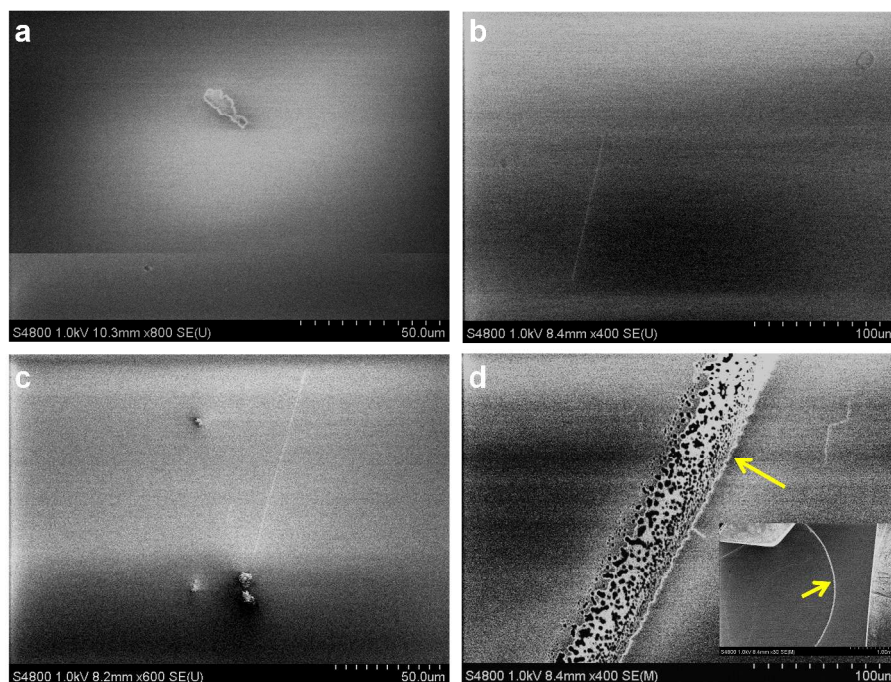


Figure S4 Effect of the pretreatment of molecule-end-caps for nanotube growth. SEM images of nanotubes growth from $C_{50}H_{10}$ after (a) 300 °C, (b) 400 °C, and (c) 500 °C air treatment. No water vapour treatment was used in these conditions. (d) After 900 °C water vapor treatment but without air treatment. In all these conditions, only sparse nanotubes grew.

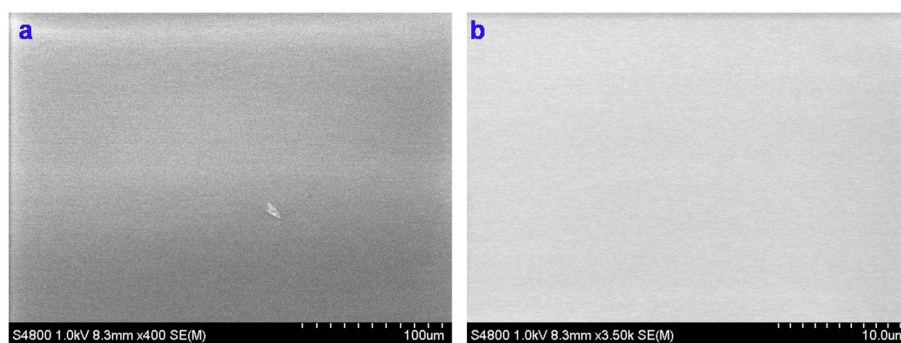


Figure S5 Control experiments. (a) Low and (b) high magnification SEM images of the blank quartz substrate after air and water vapour treatment followed by attempted CVD growth, showing no growth of nanotubes in the absence of the $C_{50}H_{10}$ molecules.

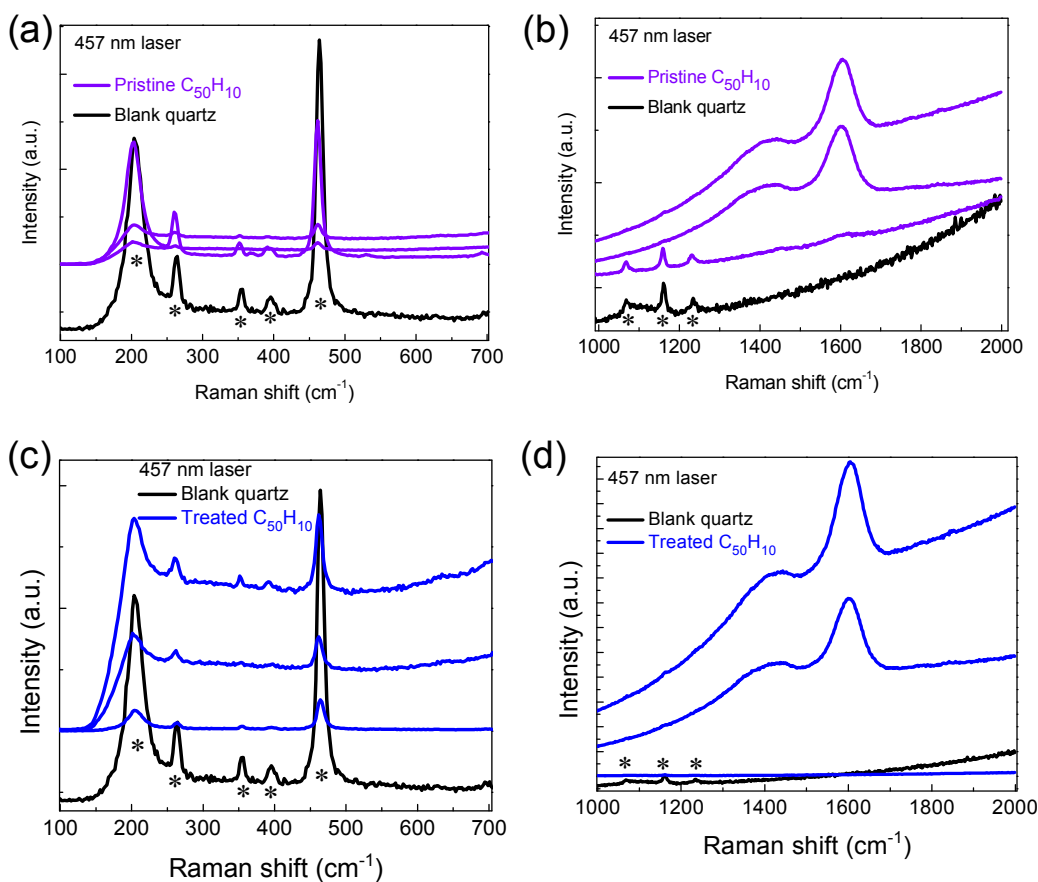


Figure S6 Raman spectra of pristine and air-treated $C_{50}H_{10}$ molecules. (a) Short wavelength region (100-700 cm^{-1}), and (b) Long wavelength region (1000-2000 cm^{-1}) of the pristine $C_{50}H_{10}$. (c) Short wavelength region, and (d) Long wavelength region of the air-treated $C_{50}H_{10}$. The treatment was air oxidation at 500 $^{\circ}C$ for 30 min. All the peaks denoted by * originated from the quartz substrates. It can be seen that there is no peak from either pristine or treated $C_{50}H_{10}$ molecules in the 100-700 cm^{-1} range. For the treated molecules, the Raman intensity was much weaker than pristine ones, and much longer integration time was used to collect the Raman spectra. We also carried out Raman studies of $C_{50}H_{10}$ molecules under 514 nm and 633 nm laser excitation, and the peaks were too weak to be clearly resolved.

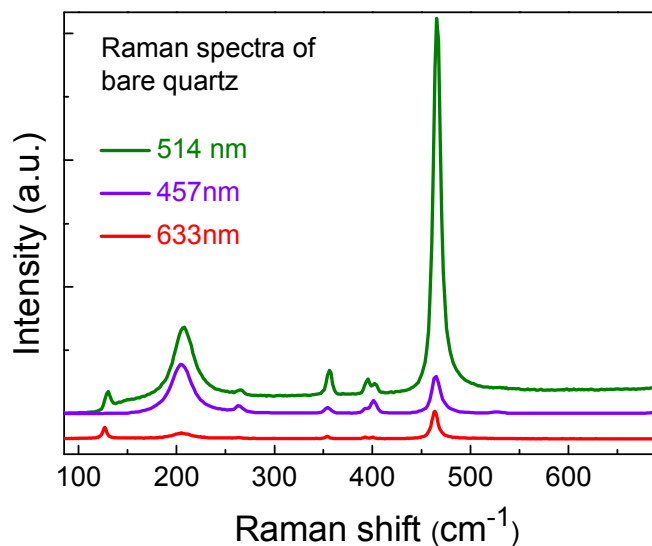


Figure S7 Raman spectra of the bare quartz substrate under different lasers.

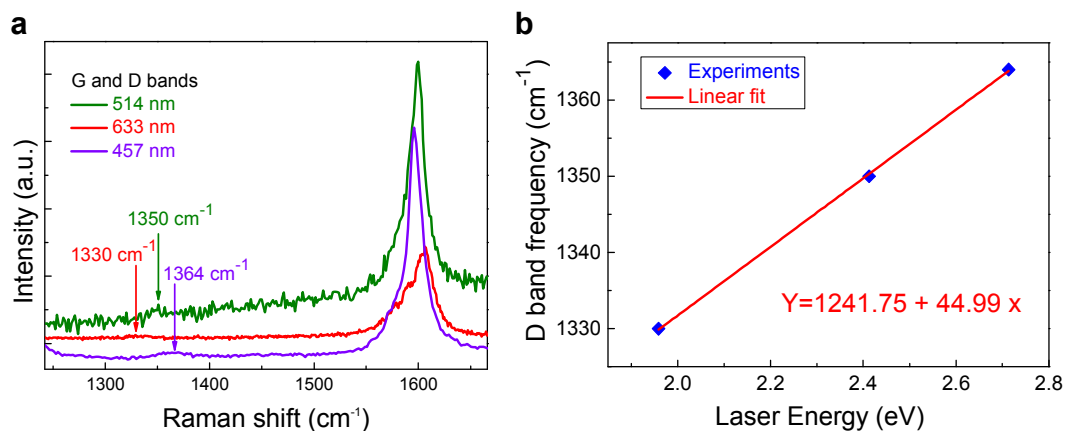


Figure S8 (a) Raman G-band and D-band spectra of the SWCNTs grown from $C_{50}H_{10}$ based on three lasers. The high quality of the SWCNTs is confirmed by all three lasers. (b) A laser energy-dependent shift of the D-band frequency, i.e., the dispersive behavior, is observed and is consistent with early reports on the Raman spectra of nanotubes and graphene.^{1,2} The dispersion relationship is $(\partial\omega_D/\partial E_{\text{laser}}) = 45 \text{ cm}^{-1}/\text{eV}$.

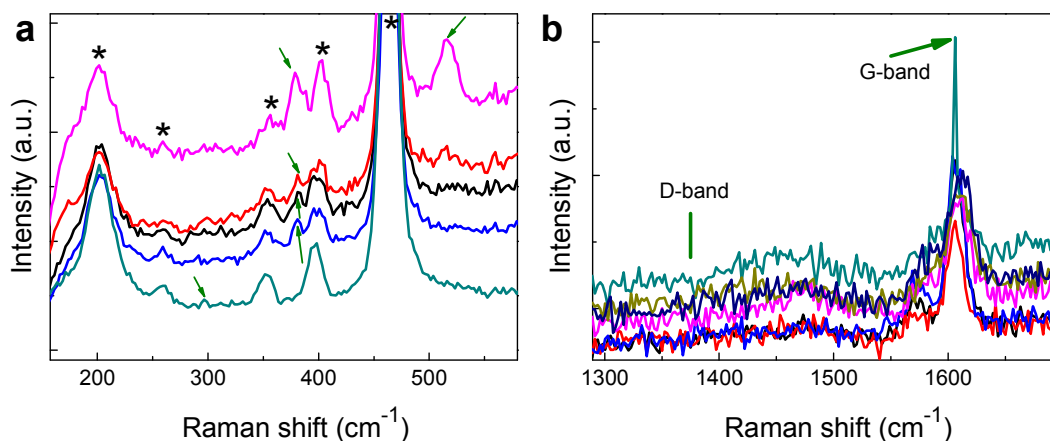


Figure S9 Raman spectra of as-grown SWCNTs taken from a 405 nm laser (CL-2000 Diode pumped CrystaLaser LC, Renishaw, UK). Figure S9a is the RBM regime and Figure S9b is the D-band and G-band regime. In Figure S9a, the six green arrows indicate six RBMs while all the other peaks (indicated by black asterisk *) originate from the quartz substrate. No peaks were observed at $\sim 340 \text{ cm}^{-1}$ for (5, 5) CNTs.³

Table S1. A summary of the six RBMs observed under the 405 nm laser and possible chirality index assignments based on the Kataura plot.⁴

No.	1	2	3	4	5	6
RBM (cm^{-1})	382	517	382	381	296	380
(n, m)	(6,2)/(7,1)	N.A.	(6,2)/(7,1)	(6,2)/(7,1)	N.A.	(6,2)/(7,1)

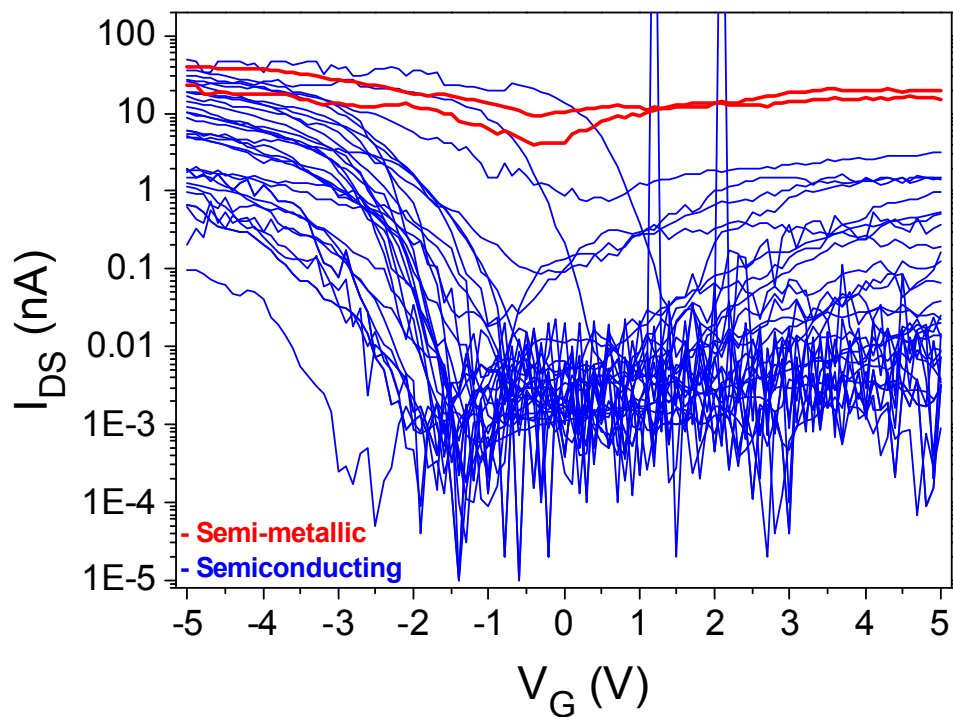


Figure S10 A summary of the transfer characteristics (I_{DS} - V_G) of all individual SWCNT FETs. The total devices number is 34 and 2 of them (red curves) show on/off ratio of <10 and are assigned to be metallic SWCNTs. Note that for true metallic SWCNTs, i.e., armchair (n, n) SWCNTs, the on/off ratio should be ~ 1 . The red curves in this figure show on/off ratios of 4.6 and 5.8, respectively. This behavior can be attributed to the so-called semi-metallic SWCNTs with a small energy band gap.⁵ We count these red curves as metallic SWCNTs.

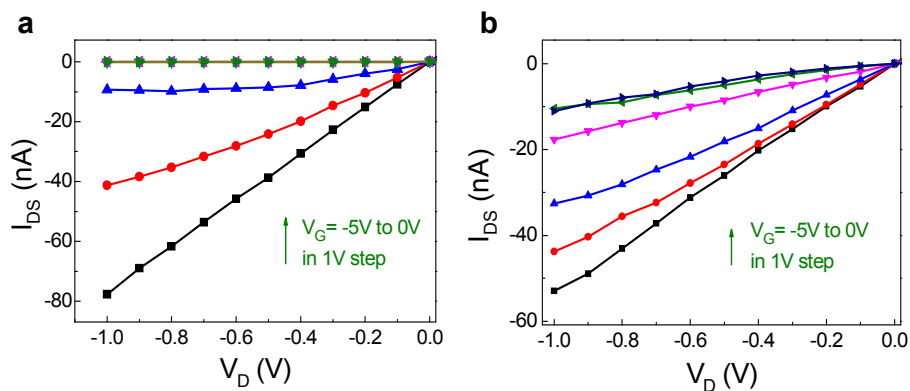


Figure S11 Output characteristics (I_{DS} - V_D) of typical semiconducting and metallic SWCNT FETs, corresponding to the same devices in Figure 4c and Figure 4d in the main text, respectively.

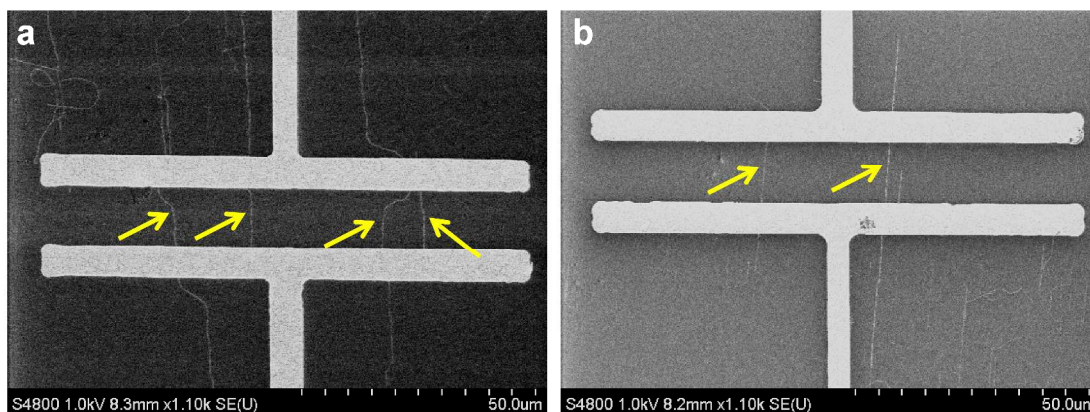


Figure S12 Low magnification SEM images of the device shown in the inset of Figure 4e (a) and Figure 4g (b). The whole channel area of the device is visible. Four SWCNTs and two SWCNTs can be clearly discerned in image a and b, respectively.

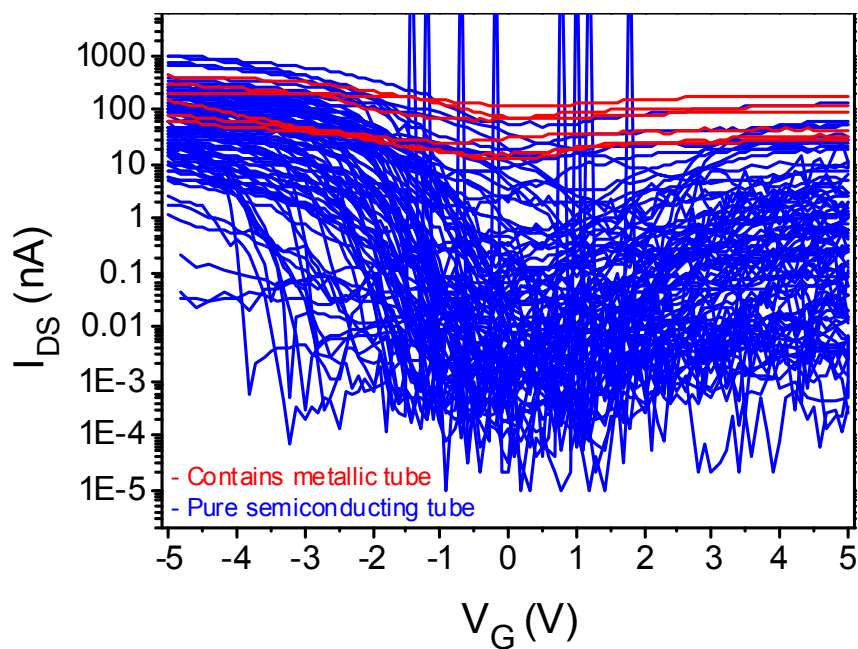


Figure S13 A summary of the transfer characteristics of all SWCNT-array-FETs. The total devices number is 93, and 6 of them (red curves) show on/off ratios of <10 and are assigned to contain metallic SWCNTs. Further electrical breakdown experiments of all these devices identified that for the 6 metallic FETs, the on/off ratio increased substantially after the breakdown of the first metallic SWCNT at the positive gate voltage, indicating only one metallic SWCNT in each of these six devices. For the 87 semiconducting devices, we found that they contain 2-5 parallel SWCNTs in the channel and the electrical breakdown combining SEM imaging can identify all of them. Overall, for these SWCNT array devices, we identified a total of 232 semiconducting SWCNTs and 6 metallic ones.

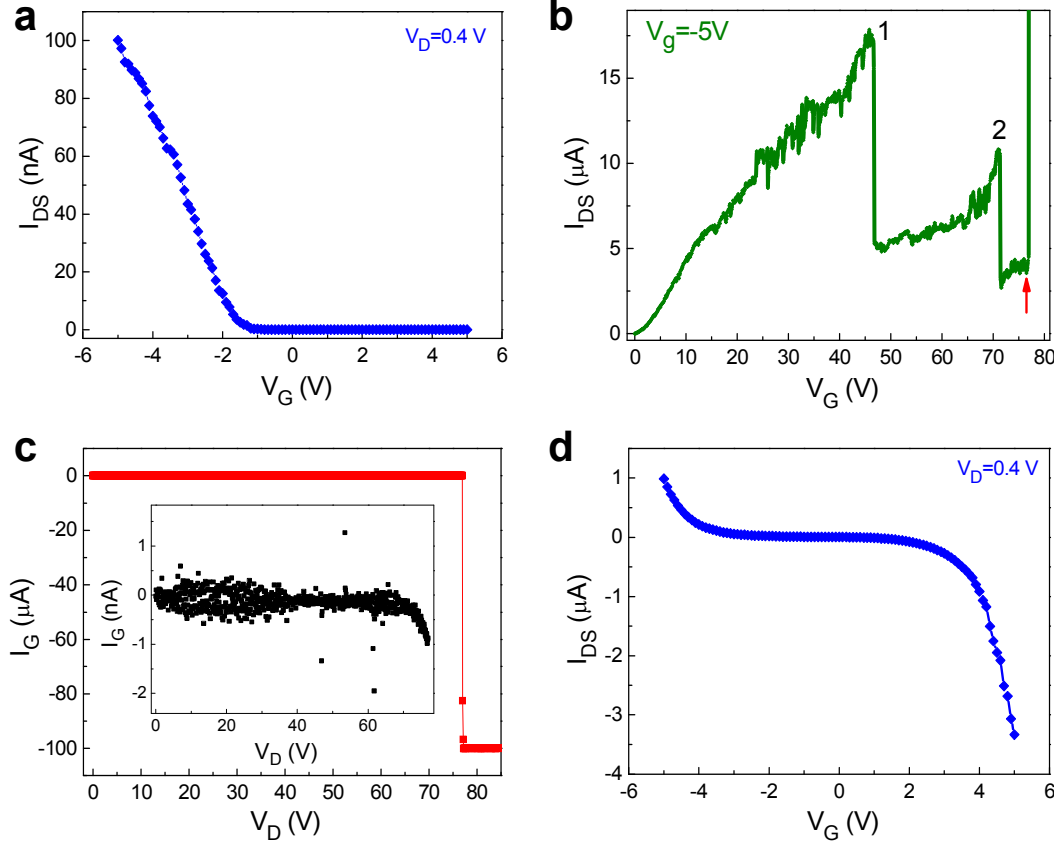


Figure S14 Electrical breakdown^{6,7} of an all-semiconducting SWCNT array FETs. (a) Transfer characteristic of the device before breakdown. (b) The breakdown experiments of this device at a $V_G = -5$ V. The gate dielectric (90 nm SiO_2) was damaged at a $V_D = 77$ V (red arrow). This device was considered to have at least three semiconducting SWCNTs in the channel and is counted as 3 for statistical analysis. (c) Gate current (I_G) during the breakdown process. Inset is the zoom in plot with $V_D < 70$ V. (d) Transfer characteristic of the device after breakdown, showing that the device was damaged.

Table S2. A summary of the total number of SWCNTs from both individual and SWCNT array FETs

	Total devices	Total SWCNTs	Metallic SWCNTs	Semiconducting SWCNTs
Individual SWCNT FETs	34	34	2	32
SWCNT array FETs	93	238	6	232
All FETs	127	272	8	264
Semiconducting SWCNT ratio=264/272=97.1%				

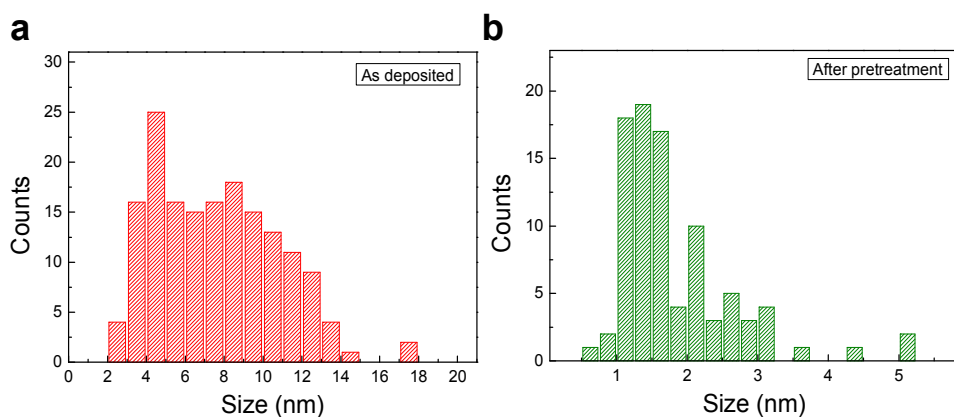


Figure S15 (a), (b) Size distributions of as deposited $C_{50}H_{10}$ molecular seeds (a) and after air and water vapour treatment (b). The average sizes of the clusters are 7.1 nm for (a) and 1.7 nm for (b).

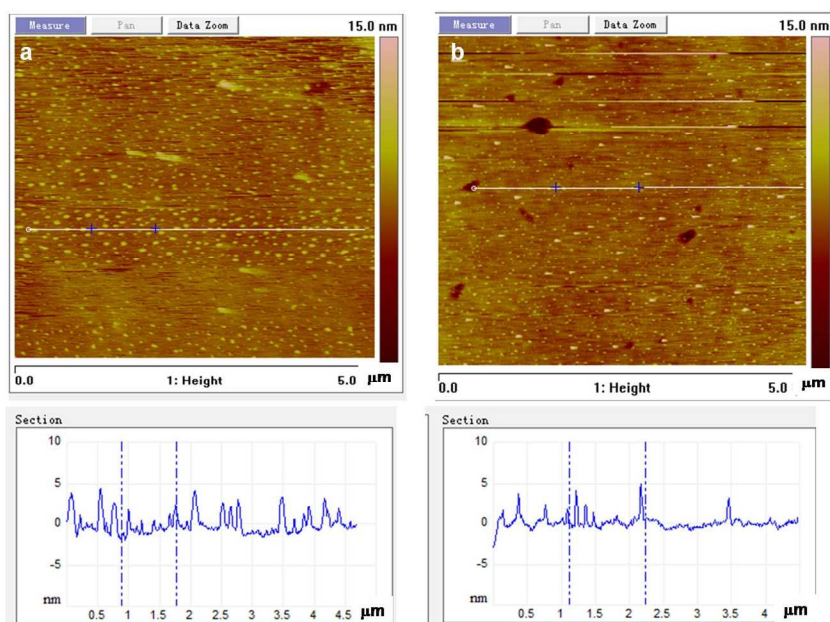


Figure S16 AFM images of the $C_{50}H_{10}$ molecules after (a) 300 °C and (b) 400 °C air treatment. The bottom panels show corresponding height profiles of the white lines in images (a) and (b).

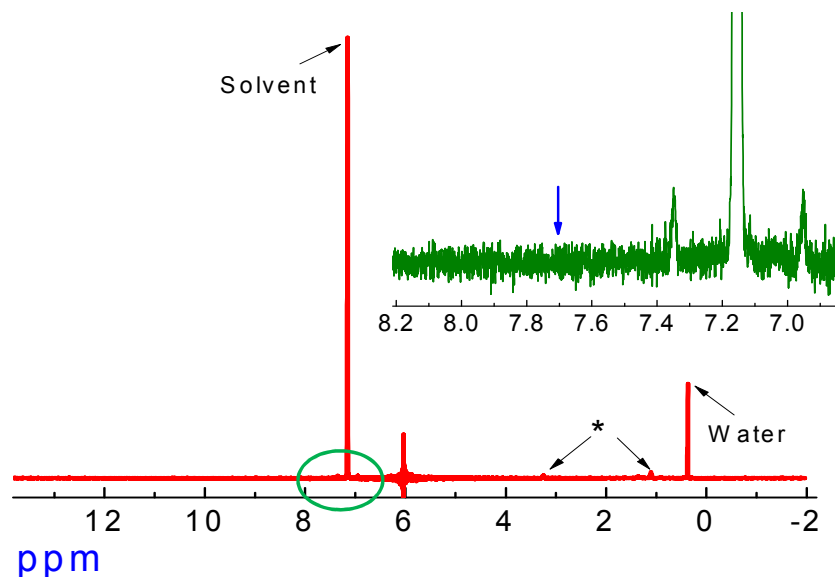


Figure S17 1H NMR (400 MHz, C_6D_6) of $C_{50}H_{10}$ after air treatment at 500 °C. Inset shows the zoom-in of 7-8 ppm area. The $\delta 7.63$ (s, 10H) peak⁸ disappeared after the treatment (blue arrow in the inset), indicating decomposition of the $C_{50}H_{10}$ molecule. The peaks indicated by black arrows originated from trace amount of diethyl ether in C_6D_6 solvent.⁹

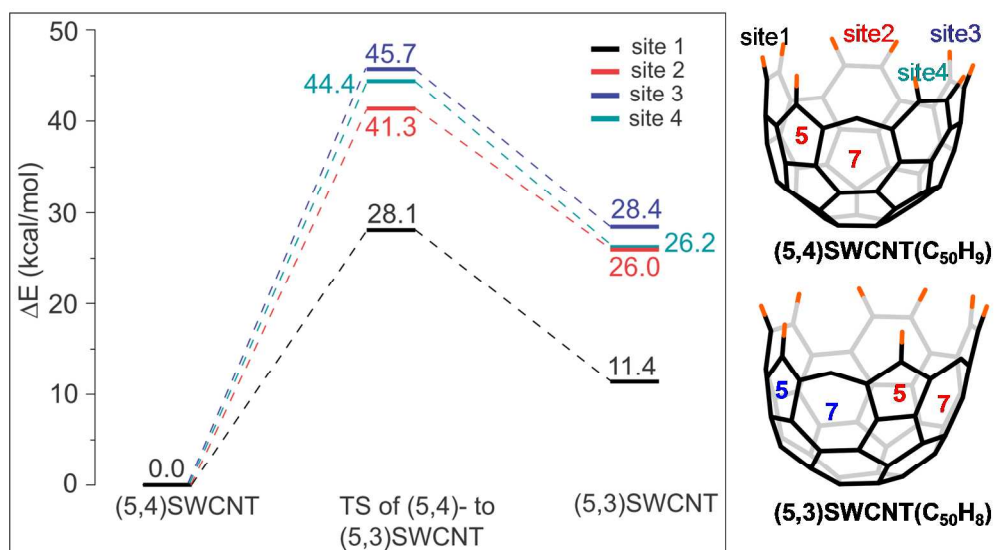


Figure S18 The relative energy profiles of the transformations from (5,4) into (5,3) SWCNT caps at different bent regions (sites), by means of conversion of adjacent hexagon-hexagon (6-6) pairs into pentagon-heptagon (5-7) defects, as reported by Smalley and Yakobson.¹⁰ The results show that the site 1, locating nearby the initial pentagon (five-member-ring, red letter), has the lowest transformation barrier to form a new pentagon-heptagon pairs (5-6 pairs, blue letter).

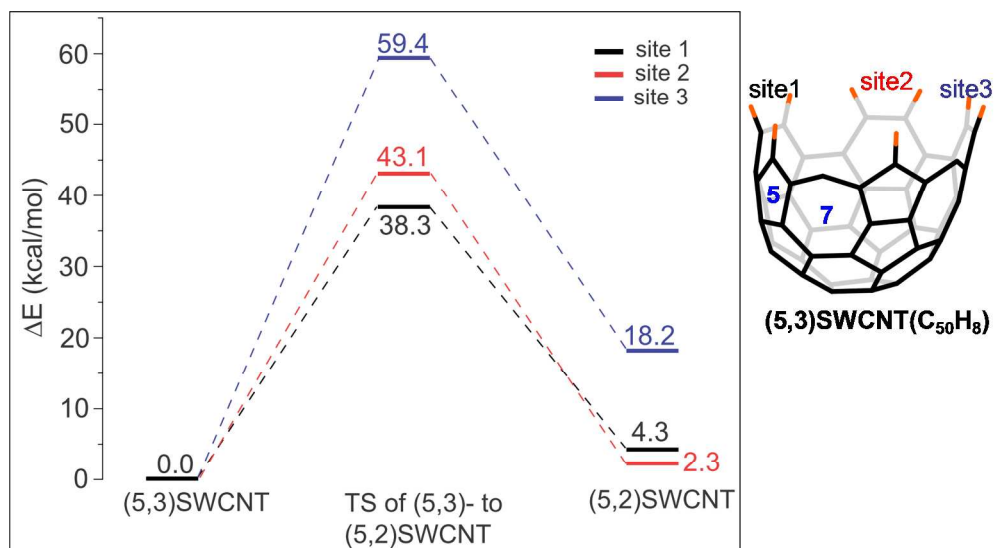


Figure S19 The relative energy profiles of the transformations from (5, 3) into (5, 2) SWCNT caps at different bent regions (sites). The results show that the site 1, locating nearby the initial pentagon, has the lowest transformation barrier to form a new 5-7 pairs.

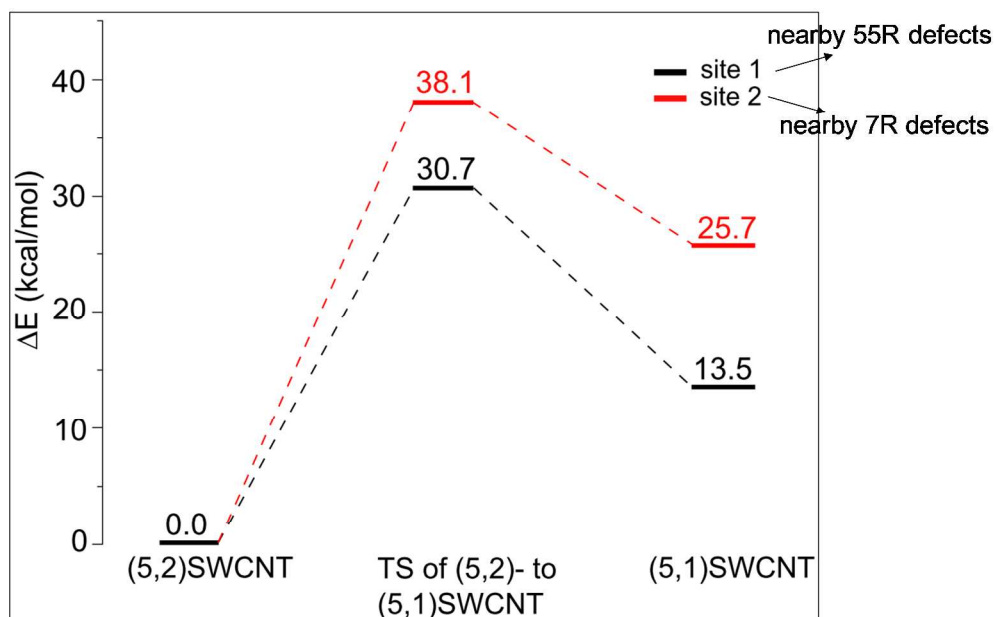


Figure S20 The relative energy profiles of the transformations from (5, 2) into (5, 1) SWCNT caps at different bent regions (sites). The results show that the site 1, locating nearby the initial pentagon, has the lowest transformation barrier to form a new 5-7 pairs.

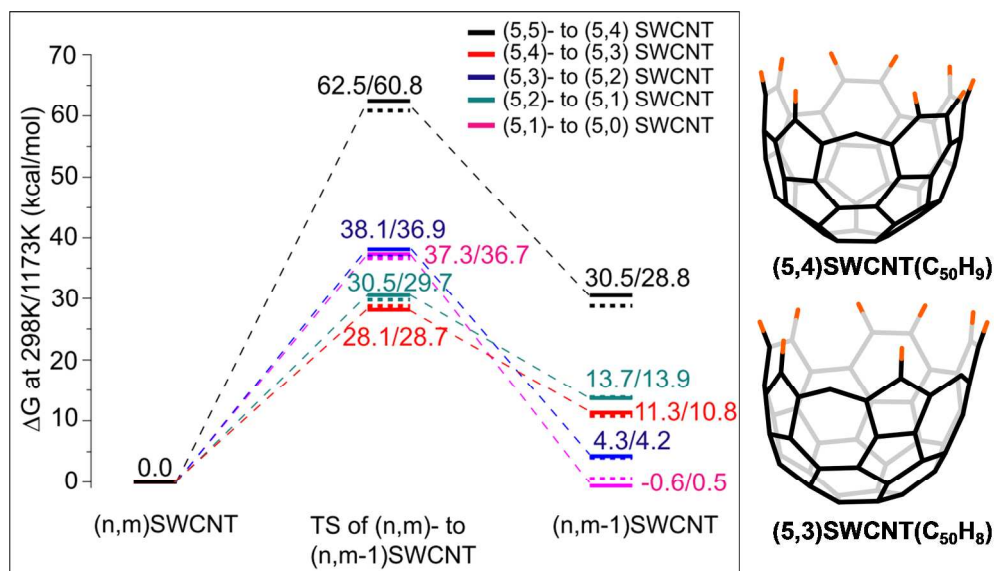


Figure S21 The relative Gibbs free energy profiles of the transformations from (5, m) into (5, m-1) SWCNT caps of C₅₀H_{m+4} (m=5, 4, 3, 2, respectively) at 298.15K (solid line) and 1173K (dash line).

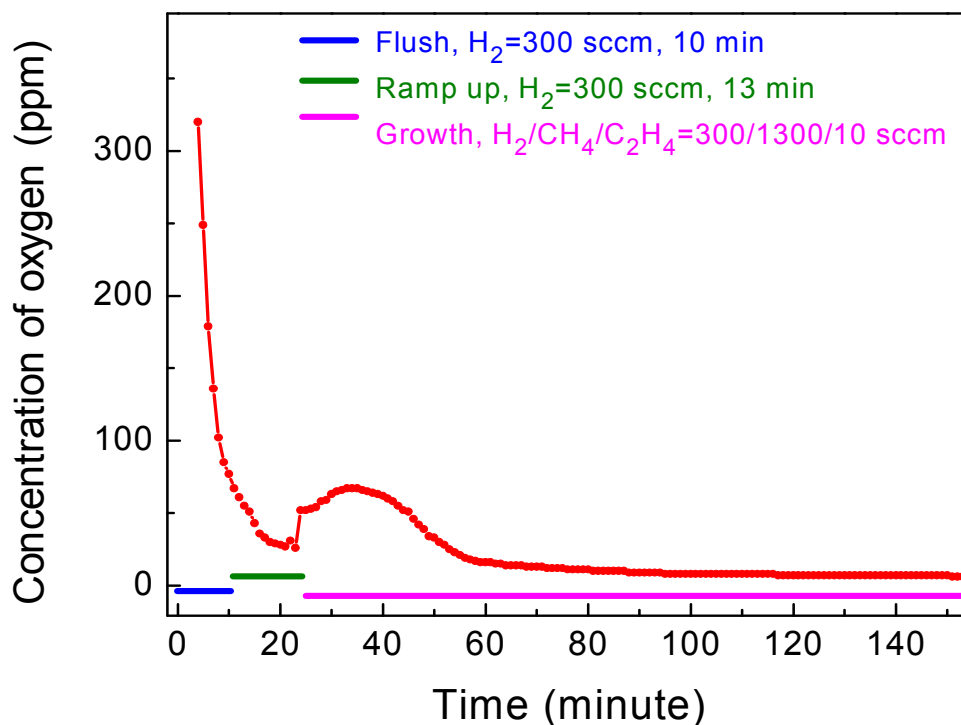


Figure S22 *In situ* measurements of oxygen concentration during SWCNT growth. The initial O₂ concentration is higher than the detection limit (1000 ppm) of the sensor. After H₂ flush (10 minutes) and furnace ramp-up (13 minutes) periods, the O₂ concentration drops to 23 ppm. The initial introduction of CH₄ and C₂H₄ increases the O₂ concentration to 77 ppm. Then, it decreases gradually and stabilizes at ~7 ppm. Overall, the highest O₂ concentration is 77 ppm during the nanotube growth process, which is significantly lower than an early study which used a few hundred ppm of O₂.¹¹

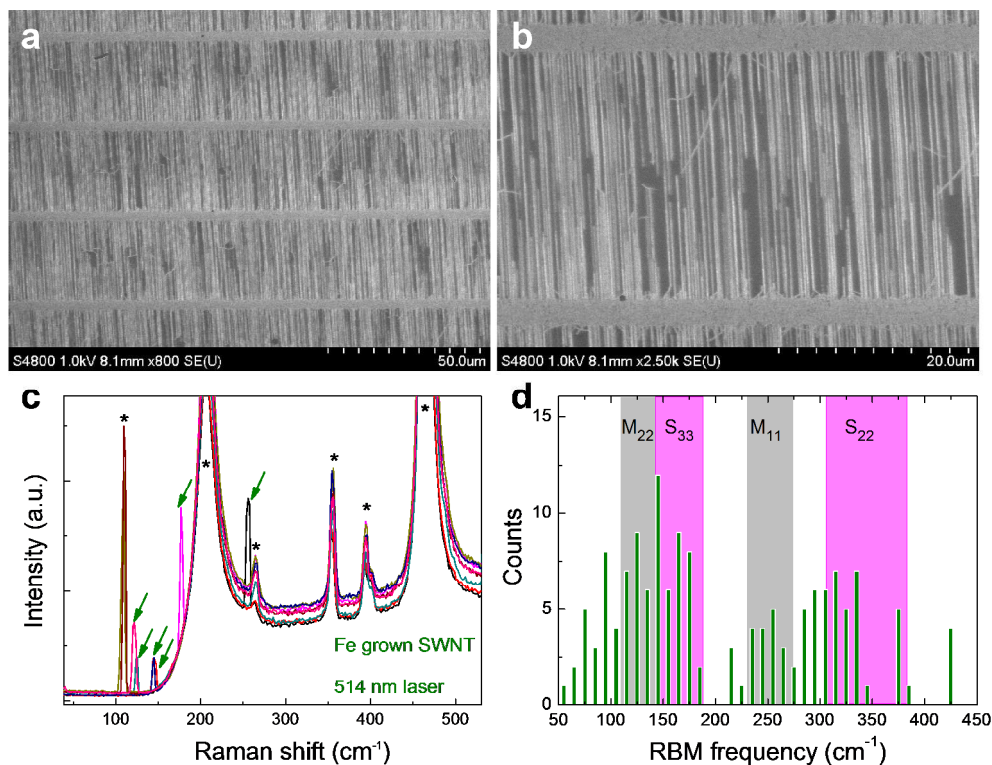


Figure S23 Comparative studies of Fe-grown SWCNTs under identical CVD conditions. (a), (b) SEM images. (c) Representative Raman spectra of nanotubes grow from Fe catalyst. The green arrows indicate RBMs while the asterisk (*) indicate peaks from the quartz substrates. (d) Statistical analysis of the RBM distribution of SWCNTs grown from Fe catalysts. The total number of RBM peaks is 151. The colored stripes of M₂₂, S₃₃, M₁₁, and S₂₂ correspond to the second electronic transition of metallic SWCNTs, the third electronic transition of semiconducting SWCNTs, the first electronic transition of metallic SWCNTs, and the second electronic transition of semiconducting SWCNTs, respectively.

References

1. Dresselhaus, M. S.; Dresselhaus, G.; Saito, R.; Jorio, A. *Physics Reports* **2005**, *409*, 47-99.
2. Jorio, A.; Saito, R.; Dresselhaus, M. S.; Dresselhaus, G. *Wiley VCH Verlag GmbH & Co. KGaA, Weinheim* **2010**.
3. Haroz, E. H.; Duque, J. G.; Lu, B. Y.; Nikolaev, P.; Arepalli, S.; Hauge, R. H.; Doorn, S. K.; Kono, J. *J. Am. Chem. Soc.* **2012**, *134*, 4461-4464.
4. http://www.ece.rice.edu/~irlabs/research/SWCNT_assignment_table.pdf.
5. Zhou, C. W.; Kong, J.; Dai, H. J. *Phys. Rev. Lett.* **2000**, *84*, 5604-5607.
6. Collins, P. C.; Arnold, M. S.; Avouris, P. *Science* **2001**, *292*, 706-709.
7. Jin, S. H.; Dunham, S. N.; Song, J. Z.; Xie, X.; Kim, J. H.; Lu, C. F.; Islam, A.; Du, F.; Kim, J.; Felts, J.; Li, Y. H.; Xiong, F.; Wahab, M. A.; Menon, M.; Cho, E.; Grosse, K. L.; Lee, D. J.; Chung, H. U.; Pop, E.; Alam, M. A.; King, W. P.; Huang, Y. G.; Rogers, J. A. *Nat. Nanotech.* **2013**, *8*, 347-355.
8. Scott, L. T.; Jackson, E. A.; Zhang, Q. Y.; Steinberg, B. D.; Bancu, M.; Li, B. *J. Am. Chem. Soc.* **2012**, *134*, 107-110.
9. Fulmer, G. R.; Miller, A. J. M.; Sherden, N. H.; Gottlieb, H. E.; Nudelman, A.; Stoltz, B. M.; Bercaw, J. E.; Goldberg, K. I. *Organometallics* **2010**, *29*, 2176-2179.
10. Smalley, R. E.; Yakobson, B. I. *Solid State Commun.* **1998**, *107*, 597-606.
11. Yu, B.; Liu, C.; Hou, P. X.; Tian, Y.; Li, S. S.; Liu, B. L.; Li, F.; Kauppinen, E. I.; Cheng, H.-M. *J. Am. Chem. Soc.* **2011**, *133*, 5232-5235.